Electronic Supplementary Information: Lighting up long-range charge-transfer states by localized plasmonic field

Zhen Xie,[a,b] Sai Duan,*[b] Chuan-Kui Wang,[a] and Yi Luo*[b,c]

S1 Methodology

When the molecule is under the spatial confined plasmon (SCP) field, the adiabatic interaction Hamiltonian for incident light is[1]

$$H'_{\omega} = \sqrt{\frac{2\pi}{\omega V}} M \sum_{i}^{N} \left[\frac{1}{2} \left(\hat{\mathbf{p}}_i \cdot \hat{\mathbf{g}} + \hat{\mathbf{g}} \cdot \hat{\mathbf{p}}_i \right) \hat{a}_{\omega} e^{(-\imath\omega+\gamma)t} + \text{H.c.} \right], \tag{S1}$$

where ω is the frequency of incident light, V is the system volume, M is the enhancement factor, N is the number of electrons, $\hat{\mathbf{p}}_i = -\imath\nabla_i$ is the momentum operator of the ith electron, $\mathbf{g}$ is the mode function of vector potential $\mathbf{A}(\mathbf{r},t)$, $\hat{a}_{\omega}$ is the annihilation operator for photon with frequency of ω, γ is a positive infinitesimal, and H.c is the hermitian conjugate. Here, the Coulomb's gauge for the vector potential is adopted:

$$\text{div}\mathbf{A}(\mathbf{r},t) = 0. \tag{S2}$$

Considering the mathematic relationship $\nabla \cdot (\mathbf{a}f) = \mathbf{a} \cdot \nabla f + f \nabla \cdot \mathbf{a}$, where $\mathbf{a}$ and f are arbitrary vector and scale functions, Eq. S1 is rewritten to

$$H'_{\omega} = \sqrt{\frac{2\pi}{\omega V}} M \sum_{i}^{N} \left[\left(\hat{\mathbf{g}} \cdot \hat{\mathbf{p}}_i \right) \hat{a}_{\omega} e^{(-\imath\omega+\gamma)t} + \text{H.c.} \right]. \tag{S3}$$

For the absorption process, once the interaction Hamiltonian is determined, the electron transition rate between two molecular states can be easily evaluated based on the Fermi's Golden rule as

$$\omega_{r \leftarrow g} \propto \frac{1}{\Delta E_{rg}} \left| \langle \Psi_r | \sum_{i} \left(\mathbf{g} \cdot \hat{\mathbf{p}}_i \right) | \Psi_g \rangle \right|^2, \tag{S4}$$

where ΔE_{rg} is the vertical excitation energy between ground and excited states, Ψ_r and Ψ_g are the excited state and the ground state, respectively.

For the scattering process, we study the scattering light that can be experimentally detected in the far field.[2] In this case, $\mathbf{g} = e^{\imath \mathbf{k} \cdot \mathbf{r}} \approx 1$ is assumed. Thus, the adiabatic interaction Hamiltonian for scattering light becomes

$$H'_{\omega_s} = \sqrt{\frac{2\pi}{\omega_s V}} \sum_{i}^{N} (\hat{\mathbf{p}}_i \hat{a}^{\dagger}_{\omega_s} e^{(\imath\omega_s+\gamma)t} + \text{H.c.}), \tag{S5}$$

where ω_s is the frequency of scattering light, and $\hat{a}^{\dagger}_{\omega_s}$ is creation operator for photon with frequency of ω_s.

The Raman process consists of the absorption (absorbing an incident σ-quantum) and spontaneous emission (emitting a scattering ρ-quantum). Analogy to the elegant Albrecht's Raman theory[3], the general polarizability for resonant Raman images can be expressed by[1]

$$\alpha_{fi,\rho\sigma} = A_{\rho\sigma} + B_{\rho\sigma}, \tag{S6}$$

[a] Shandong Province Key Laboratory of Medical Physics and Image Processing Technology, School of Physics and Electronics, Shandong Normal University, Jinan 250014, China.
[b] Department of Theoretical Chemistry and Biology, School of Biotechnology, Royal Institute of Technology, S-106 91 Stockholm, Sweden. E-mail: said@theochem.kth.se.
[c] Hefei National Laboratory for Physical Science at the Microscale, University of Science and Technology of China, Hefei, 230026 Anhui, China. E-mail: yiluo@ustc.edu.cn

where

$$A_{\rho\sigma} = \frac{1}{\omega\omega_s}\left[\langle\Psi_g|\hat{V}_\rho^\dagger|\Psi_r\rangle\langle\Psi_r|\hat{V}_\sigma|\Psi_g\rangle\sum_{v^r=0}^{\infty}\frac{\langle v^f|v^r\rangle\langle v^r|v^i\rangle}{\omega_{e^rv^r:e^gv^i}-\omega-\imath\gamma}\right]+\mathrm{NRT}$$

$$B_{\rho\sigma} = \frac{1}{\omega\omega_s}\sum_k\left[\frac{\partial\langle\Psi_g|\hat{V}_\rho^\dagger|\Psi_r\rangle}{\partial Q_k}\langle\Psi_r|\hat{V}_\sigma|\Psi_g\rangle\sum_{v^r=0}^{\infty}\frac{\langle v^f|Q_k|v^r\rangle\langle v^r|v^i\rangle}{\omega_{e^rv^r:e^gv^i}-\omega-\imath\gamma}\right. \tag{S7}$$

$$\left.+\langle\Psi_g|\hat{V}_\rho^\dagger|\Psi_r\rangle\frac{\partial\langle\Psi_r|\hat{V}_\sigma|\Psi_g\rangle}{\partial Q_k}\sum_{v^r=0}^{\infty}\frac{\langle v^f|v^r\rangle\langle v^r|Q_k|v^i\rangle}{\omega_{e^rv^r:e^gv^i}-\omega-\imath\gamma}\right]+\mathrm{NRT},$$

with

$$\hat{V}_\sigma = \sum_i^N(g_\sigma\hat{p}_{i,\sigma})$$

$$\hat{V}_\rho^\dagger = \sum_i^N\hat{p}_{i,\rho}. \tag{S8}$$

Here, $A_{\rho\sigma}$ and $B_{\rho\sigma}$ represent Franck-Condon and Herzberg-Teller terms, respectively. $|v^i\rangle$ and $|v^f\rangle$ are the initial and final vibrational states in ground state $|\Psi_g\rangle$, $|v^r\rangle$ is the vibrational state in resonant excited state $|\Psi_r\rangle$, $\omega_{e^rv^r:e^gv^i}$ is the frequency difference between $|\Psi_r\rangle|v^r\rangle$ and $|\Psi_g\rangle|v^i\rangle$, Q_k is the vibrational normal modes, and NRT is the nonresonant term. We should stress that, for a forbidden Franck-Condon emission process, both the A term and the second term of the B term are zero owing to the unmodified emission operator $\hat{V}_\rho^\dagger$ ($\mathbf{g}\approx 1$), *i.e,* the forbidden transition $\langle\Psi_g|\hat{V}_\rho^\dagger|\Psi_r\rangle$. While the $\frac{\partial\langle\Psi_g|\hat{V}_\rho^\dagger|\Psi_r\rangle}{\partial Q_k}$ in the first term of the B term is non-zero. Therefore, the intensity of the resonant Raman depends on the first term of the B term, which is proportional to the **g**-modified $\langle\Psi_r|\hat{V}_\sigma|\Psi_g\rangle$.

S2 Computational details

In practical calculations, the adsorbed sample molecule constructed by the tetrathiafulvalene (TTF) as donor (D) and the 7,7′,8,8′-tetracyano-p-quinodimethane (TCNQ)-type bithienoquinoid as acceptor (A) on Au(111) surface is studied. Using the Vienna ab initio simulation package,[4] the periodic boundary condition (PBC) model was employed to optimize geometrical and electronic structures at the Perdew-Burke-Ernzerhof (PBE) functional level[5]. To consider the long-range dispersion correction, the D3 method[6] was applied. We used the projector augmented-wave (PAW) pseudopotentials[7,8] to describe the core electrons and the wavefunctions were expanded by the plane-wave basis sets with a 400 eV energy cutoff. The Methfessel and Paxton method[9] with a broadening factor of 0.1 eV was adopted for improving convergence of the electronic structure calculations with the total energies extrapolated to 0 K. The dipole correction[10,11] was also considered to avoid artificial interactions. For the k-point sampling, a 2×2×1 mesh of the Monkhorst-Pack grid[12] was used, generating 4 k points in the irreducible Brillouin zone integration. Specifically, we calculated lattice constant of Au at PBE functional level to be 4.146 Å, which nicely reproduces the experimental value of 4.086 Å[13]. Based on the calculated lattice constant, three layers of ($6\sqrt{3}\times10$) supercell of the Au(111) slab was used to simulate a large enough Au surface. Enough vacuum layer ($>$ 35 Å) was added along the z axis in the supercell. During the geometry optimization, the bottom two layers of the substrate were fixed while all other atoms could relax until the force on each atom was less than 0.02 eV/ Å.

When the molecule is adsorbed on the substrate, evaluation of the z and zz component are adequate for the absorption and Raman processes, respectively.[14] We expanded the z component of the amplitude distribution of the SCP by a set of Gaussian functions, i.e.,

$$g_z = \sum_D\sum_{l,m,n}\sum_\alpha c_{\alpha,D}^{lmn}g_{\alpha,D}^{lmn}, \tag{S9}$$

where

$$g_{\alpha,D}^{lmn} = (x-x_D)^l(y-y_D)^m(z-z_D)^ne^{-\alpha(\mathbf{r}-\mathbf{r}_D)^2} \tag{S10}$$

is a Gaussian function localized at the center $\mathbf{r}_D$ with exponent α, $c_{\alpha,D}^{lmn}$ is the corresponding coefficient, and the superscript "lmn" represent the angular momentum of Cartesian Gaussian functions. The s-type Gaussian functions are considered for

$g^{lmn}_{\alpha,D}$. The size of plasmon was determined by the full width at half maximum (fwhm) of the Gaussian function, setting the x and y components to 3 Å for $g^{000}_{\alpha,D}$. While the z component was set to infinite ($\alpha_z = 0$ Å), in which case the Coulomb's gauge is automatically fulfilled.[1] Thus, the distribution of plasmon field is simulated to be a Gaussian cylinder. Based on the optimized structures in PBC model, the coordinates of the adsorbed triadic molecule were extracted considering the weak interaction between the adsorbate and Au(111) surface. Employing the Gaussian suite of program[15], we calculated the excited states for the triad by the time-dependent density function theory (TDDFT) at B3LYP level[16] with TZVP basis set[17], which is proposed to accurately predict the electronic absorption spectrum of this experimental D-π-A molecule[18]. The calculated results of transition velocity dipole moments, vertical excitation energies as well as the coefficients of excitation and de-excitation were extracted from the Gaussian program. All the ultraviolet-visible (UV-vis) spectra under SCP field and Raman images were calculated by the "First-principles Approaches for Surface and Tip Enhanced Raman Scattering (FASTERS)" program[19].

S3 Different functionals in predicting experimental band gap and ultraviolet-visible spectrum of D-π-A

The band gap of experimental D-π-A molecule in dimethylformamide (DMF) was calculated by subtracting the vertical electron affinity (EA) from the vertical ionization Potential (IP). The solvation effects were taken into account by the conductor-like polarized continuum model (CPCM). As seen in Table S1, all three functionals employed in the main text provide similar band gap in vacuum. However, when the solvation effects are considered, ωB97XD gives around 1.4 eV overestimated IP than both B3LYP and CAM-B3LYP, which results in an inaccurate band gap for the D-π-A molecule in DMF. The calculated ultraviolet-visible spectra of the experimental D-π-A molecule at CAM-B3LYP and ωB97XD levels are depicted in Fig. S2. Both functionals cannot predict the absorption band around 1.5 eV. It should be emphasized that this band has been unambiguously assigned as the short-range charge-transfer transition in the previous experiments because it could not be observed for the solo acceptor or donor fragment.[18]

Table S1 B3LYP/CAM-B3LYP/ωB97XD Calculated Vertical Ionization Potential (IP), Vertical Electron Affinity (EA) and Band Gap (IP−EA) of Experimental D-π-A Triadic Molecule in DMF with TZVP Basis Set. All values are in eV and the experimental band gap of 0.52 eV for this triad in DMF solution is determined by cyclic voltammetry in Ref. 18 The values without considering the solvent effect is also given in parentheses.

Functionals	B3LYP	CAM-B3LYP	ωB97XD	Experiment
IP	4.94 (6.58)	5.17 (6.85)	6.57 (6.83)	
EA	4.57 (3.59)	4.73 (3.78)	4.74 (3.78)	
IP−EA	0.37 (2.99)	0.44 (3.07)	1.83 (3.05)	0.52

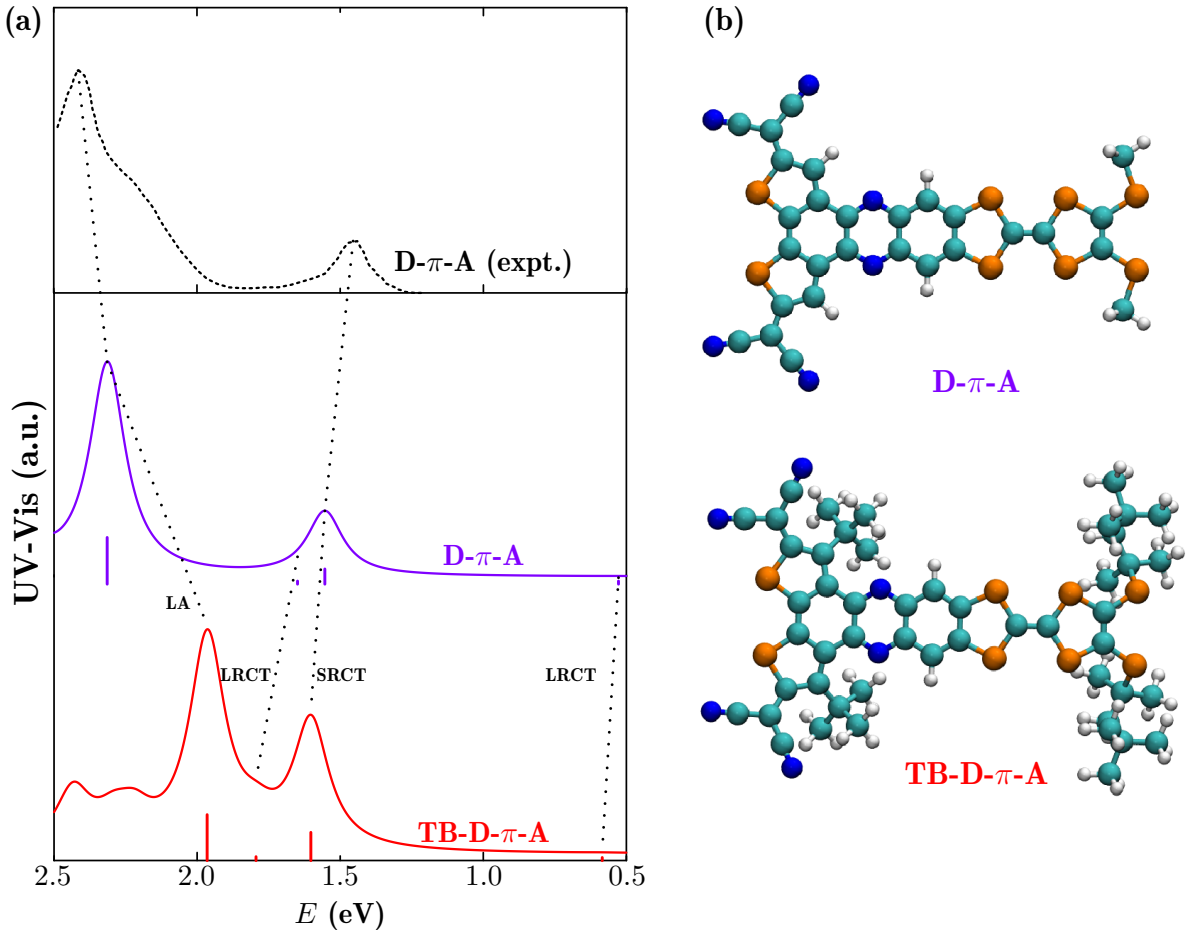

Fig. S1 (a) Calculated ultraviolet-visible spectra of the freely rotated D-π-A and TB-D-π-A molecules at B3LYP level in TZVP basis set with the geometry structures shown in (b). Experimental spectrum is shown for D-π-A molecule on the top of the Fig. S1 a. All calculated spectra were broadened by a Lorentzian function with a fwhm of 0.1 eV, and LA, LRCT and SRCT represent the local acceptor, long-range CT and short-range CT excitations, respectively.

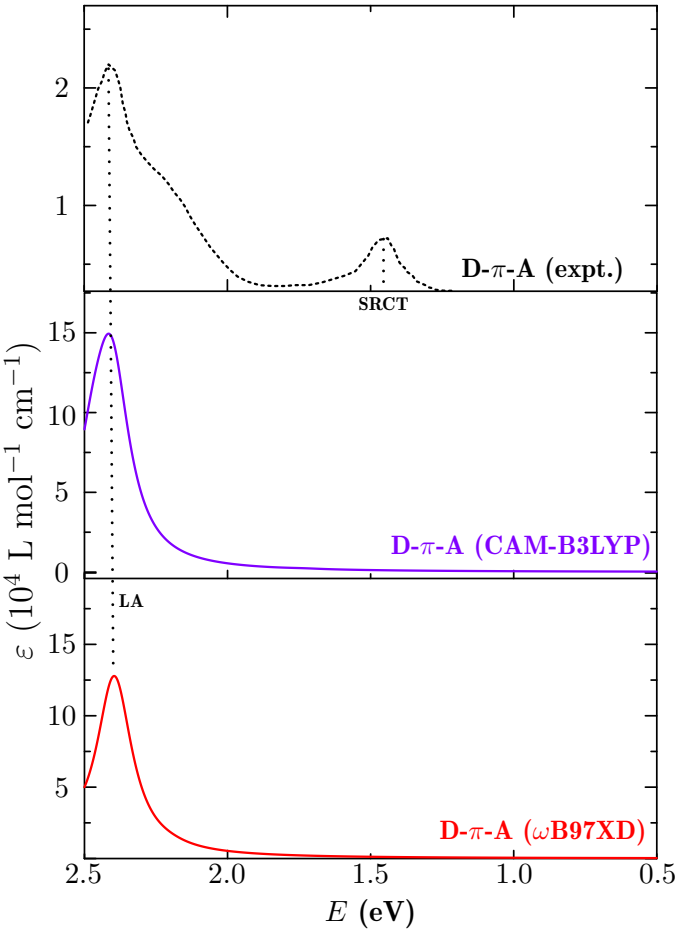

Fig. S2 Calculated ultraviolet-visible spectra of the experimental D-π-A molecule at CAM-B3LYP (middle, purple) and ωB97XD (bottom, red) levels in TZVP Basis Set. Experimental spectrum is shown on the top of the Fig. S2. All calculated spectra were broadened by a Lorentzian function with a fwhm of 0.1 eV. LA and SRCT represent the local acceptor and short-range CT excitations, respectively.

S4 Excited states and SCP spectra

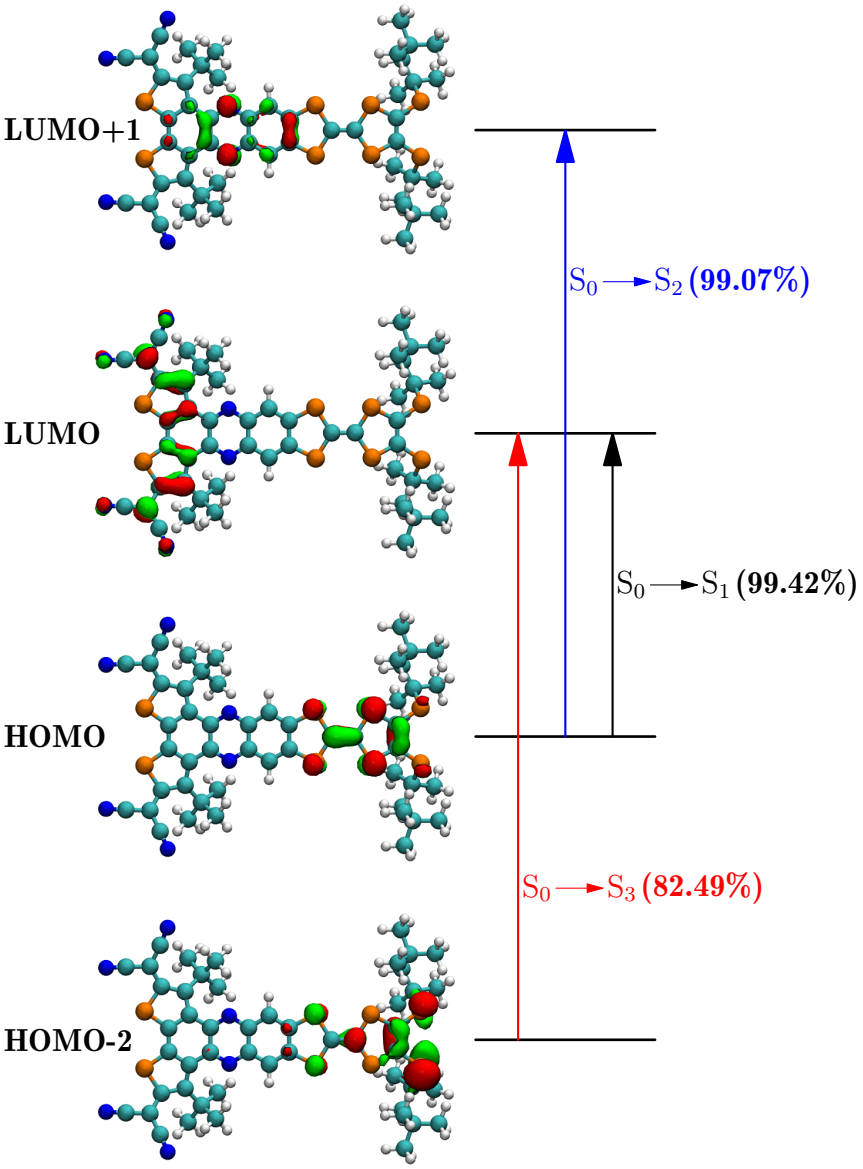

Fig. S3 Selected frontier molecular orbitals and the indication of their major participation with contribution coefficients in the first three CT excitations, and the absolute value of isosurface is 0.040.

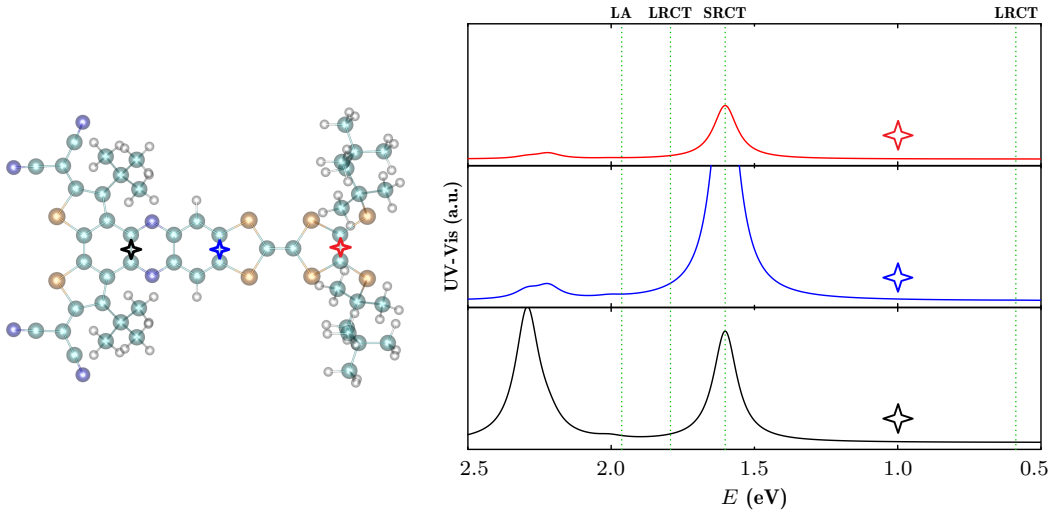

Fig. S4 Calculated UV-vis spectra of the triadic molecule (right) under a 3 Å SCP field located at representative color-coded positions marked by star with overlay of the adsorbate (left). All calculated spectra were broadened by a Lorentzian function with a fwhm of 0.1 eV. LA, LRCT and SRCT represent the local acceptor, long-range CT and short-range CT excitations, respectively.

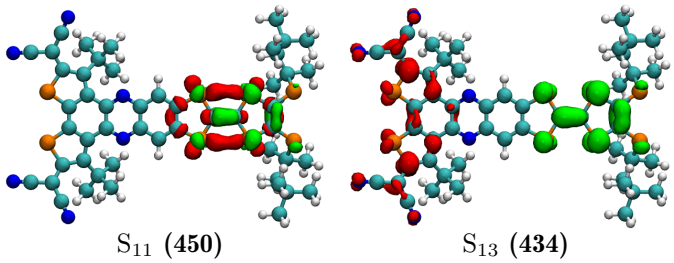

Fig. S5 Charge density differences for the local donor excited state S_{11} and the representative long-range CT state S_{13} with the matched incident light energy in nm in parenthesis, where red and green parts correspond to the electron accumulation and depletion, respectively, and the absolute value of isosurface is 0.002.

S5 Resonant raman images for CT states

Table S2 Differential Bader Charge in A (Acceptor), π (π-Bridge), and D (Donor) Fragments between S_0 and Excited States

Excited states	S_1	S_2	S_3	S_4	S_{11}	S_{13}
A	-0.54	-0.19	-0.42	-0.10	-0.04	-0.47
π	0.07	-0.11	0.05	-0.01	-0.03	0.04
D	0.47	0.30	0.37	0.11	0.07	0.43

Table S3 Projected Transition Dipole Moment along the transition direction between S_0 and Excited States into D (Donor), π (π-Bridge), and A (Acceptor) Fragments. The largest contribution and those more than 40% of the largest in absolute value are shown in bold font.

From	To	S_1	S_2	S_3	S_4	S_{11}	S_{13}
D	D	-0.0043	**0.1015**	-0.0040	-0.0066	**0.0334**	**-0.0177**
D	π	0.0030	-0.0070	-0.0056	-0.0039	0.0003	0.0063
D	A	0.0000	0.0001	-0.0000	-0.0001	-0.0001	-0.0001
π	D	-0.0034	0.0093	0.0041	0.0031	0.0008	-0.0012
π	π	**0.0218**	**0.0491**	-0.0222	-0.0131	0.0121	**0.0151**
π	A	0.0013	0.0053	-0.0104	0.0009	0.0023	0.0007
A	D	-0.0000	-0.0002	0.0000	0.0001	0.0001	0.0001
A	π	-0.0078	-0.0039	0.0027	0.0040	0.0044	-0.0081
A	A	-0.0071	0.0220	**0.1097**	**0.2642**	-0.0041	**0.0229**

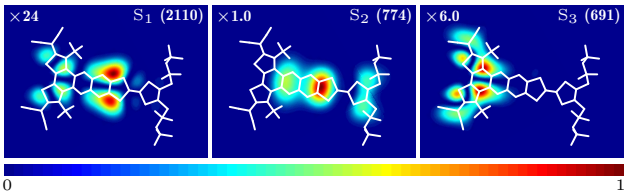

Fig. S6 Resonant Raman images with 3 Å plasmons for the corresponding CT states with the matched light energy in nm in parenthesis. The inserted values represent the scale factor for the corresponding image.

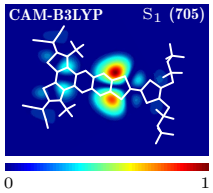

Fig. S7 Calculated resonant Raman images at CAM-B3LYP level with 3 Å plasmons for the first excited state S_1 with the matched light energy in nm in parenthesis.

Based on the assignment of fragments D, A as well as π from Raman images, the projected transition dipole moment along the transition direction between the ground and excited states is calculated as shown in Table S3. It could nicely reflect the moieties among the whole D-π-A molecule where Raman patterns exist. For instance, the dipole moment transitions from the ground state to the S_4 and S_{11} excitations are dominantly contributed by A-to-A and D-to-D, respectively. Thus, the resonant Raman image (Fig. 4) for the corresponding excitation S_4 (S_{11}) only has the local patterns in A (D) site of the triadic molecule. The Raman images for selected CT states are given in Fig. S6. The imaging for the short-range CT excitation (S_2) at 774 nm can show the corresponding CT process from D to π. Accordingly, the fragments D and π have a considerable contribution to this CT excitation. While for the long-range CT (LRCT) states from D to A at S_1 (2110 nm) and S_3 (691 nm) excitations, the Raman images could not reflect the LRCT process. Table S3 shows that the LRCT state of S_3 "borrows" dominant intensity from locally excited acceptor. As a result, there are only patterns located in the acceptor site from the Raman image of S_3. When it comes to the LRCT state of S_1, except the main contribution of π-to-π, the dipole moment transitions from A-to-π and A-to-A also have considerable contributions to this LRCT state.

Thus, the Raman image shows bright patterns in fragment π and moderate bright patterns in fragment A. In general, only in the case that the LRCT state "borrows" considerable intensity from all the locally excited fragments of D, A and π, the LRCT state of a D-π-A molecule can be visualized in real space by tip-enhanced resonant Raman scattering.

References

1 S. Duan, G. Tian, Z. Xie and Y. Luo, *J. Chem. Phys.*, 2017, **146**, 194106.
2 S. Duan, G. Tian and Y. Luo, *J. Chem. Theory Comput.*, 2016, **12**, 4986–4995.
3 A. C. Albrecht, *J. Chem. Phys.*, 1961, **34**, 1476–1484.
4 G. Kresse and J. Furthmüller, *Phys. Rev. B*, 1996, **54**, 11169–11186.
5 J. P. Perdew, K. Burke and M. Ernzerhof, *Phys. Rev. Lett.*, 1996, **77**, 3865–3868.
6 S. Grimme, J. Antony, S. Ehrlich and H. Krieg, *J. Chem. Phys.*, 2010, **132**, 154104.
7 P. E. Blöchl, O. Jepsen and O. K. Andersen, *Phys. Rev. B*, 1994, **49**, 16223–16233.
8 G. Kresse and D. Joubert, *Phys. Rev. B*, 1999, **59**, 1758–1775.
9 M. Methfessel and A. T. Paxton, *Phys. Rev. B*, 1989, **40**, 3616–3621.
10 J. Neugebauer and M. Scheffler, *Phys. Rev. B*, 1992, **46**, 16067–16080.
11 G. Makov and M. C. Payne, *Phys. Rev. B*, 1995, **51**, 4014–4022.
12 H. J. Monkhorst and J. D. Pack, *Phys. Rev. B*, 1976, **13**, 5188–5192.
13 D. R. Lide, *Handbook of Chemistry and Physics, 87th ed.*, CRC press, 2004.
14 R. Zhang, Y. Zhang, Z. Dong, S. Jiang, C. Zhang, L. Chen, L. Zhang, Y. Liao, J. Aizpurua, Y. Luo, J. Yang and J. Hou, *Nature*, 2013, **498**, 82–86.
15 M. J. Frisch, G. W. Trucks, H. B. Schlegel, G. E. Scuseria, M. A. Robb, J. R. Cheeseman, G. Scalmani, V. Barone, B. Mennucci, G. A. Petersson, H. Nakatsuji, M. Caricato, X. Li, H. P. Hratchian, A. F. Izmaylov, J. Bloino, G. Zheng, J. L. Sonnenberg, M. Hada, M. Ehara, K. Toyota, R. Fukuda, J. Hasegawa, M. Ishida, T. Nakajima, Y. Honda, O. Kitao, H. Nakai, T. Vreven, J. A. Montgomery, Jr., J. E. Peralta, F. Ogliaro, M. Bearpark, J. J. Heyd, E. Brothers, K. N. Kudin, V. N. Staroverov, R. Kobayashi, J. Normand, K. Raghavachari, A. Rendell, J. C. Burant, S. S. Iyengar, J. Tomasi, M. Cossi, N. Rega, J. M. Millam, M. Klene, J. E. Knox, J. B. Cross, V. Bakken, C. Adamo, J. Jaramillo, R. Gomperts, R. E. Stratmann, O. Yazyev, A. J. Austin, R. Cammi, C. Pomelli, J. W. Ochterski, R. L. Martin, K. Morokuma, V. G. Zakrzewski, G. A. Voth, P. Salvador, J. J. Dannenberg, S. Dapprich, A. D. Daniels, Ö. Farkas, J. B. Foresman, J. V. Ortiz, J. Cioslowski and D. J. Fox, *Gaussian 09 Revision D. 01*, 2009, Gaussian Inc. Wallingford CT.
16 A. D. Becke, *J. Chem. Phys.*, 1993, **98**, 1372–1377.
17 K. Eichkorn, F. Weigend, O. Treutler and R. Ahlrichs, *Theor. Chem. Acc.*, 1997, **97**, 119–124.
18 X. Guégano, A. L. Kanibolotsky, C. Blum, S. F. L. Mertens, S.-X. Liu, A. Neels, H. Hagemann, P. Skabara, S. Leutwyler, T. Wandlowski, A. Hauser and S. Decurtins, *Chem. Eur. J*, 2009, **15**, 63–66.
19 S. Duan, G. Tian and Y. Luo, *First-principles Approaches for Surface and Tip Enhanced Raman Scattering (FASTERS) Version 1.0*, Royal Institute of Technology, Stockholm, Sweden, 2016.